Dramatic improvement of formability in Mg-3Al-1Sn-0.5Ca-0.1Sm alloy via Mn microalloying combined with high temperature rolling

Wang, Shi Chao; Chen, Si Yu; Jin, Zhong Zheng; Ma, Xiao; Jia, Hai-Long ; Zhu, Jia Ning; Li, Chun Yuan; Zha, Min; Wang, Hui Yuan

DOI
10.1016/j.jma.2024.06.022

Publication date
2025

Document Version
Final published version

Published in
Journal of Magnesium and Alloys

Citation (APA)
Wang, S. C., Chen, S. Y., Jin, Z. Z., Ma, X., Jia, H.-L., Zhu, J. N., Li, C. Y., Zha, M., & Wang, H. Y. (2025). Dramatic improvement of formability in Mg-3Al-1Sn-0.5Ca-0.1Sm alloy via Mn microalloying combined with high temperature rolling. *Journal of Magnesium and Alloys*, *13*(4), 1630-1645. https://doi.org/10.1016/j.jma.2024.06.022

Available online at www.keaipublishing.com/en/journals/journal-of-magnesium-and-alloys/

ScienceDirect

Journal of Magnesium and Alloys 13 (2025) 1630–1645

www.elsevier.com/locate/jma

Full Length Article

Dramatic improvement of formability in Mg-3Al-1Sn-0.5Ca-0.1Sm alloy via Mn microalloying combined with high temperature rolling

Shi-Chao Wang[d], Si-Yu Chen[d], Zhong-Zheng Jin[b,*], Xiao Ma[d], Hai-Long Jia[d,e], Jia-Ning Zhu[c], Chun-Yuan Li[d], Min Zha[a,d,e,*], Hui-Yuan Wang[d,e]

[a] *State Key Laboratory of Superhard Materials, Jilin University, Changchun, 130012, PR China*
[b] *Key Laboratory of UV-Emitting Materials and Technology of Ministry of Education, Northeast Normal University, Changchun 130024, PR China*
[c] *Department of Materials Science and Engineering, Delft University of Technology, the Netherlands*
[d] *Key Laboratory of Automobile Materials of Ministry of Education & School of Materials Science and Engineering, Nanling Campus, Jilin University, No. 5988 Renmin Street, Changchun 130025, PR China*
[e] *International Center of Future Science, Jilin University, Changchun 130012, PR China*

Received 2 February 2024; received in revised form 14 June 2024; accepted 19 June 2024
Available online 6 July 2024

Abstract

Rolled Mg-Al-Sn series alloys generally possess limited formability due to the formation of strong basal texture. Texture weakening is an effective way to enhance formability, but usually accompanied with decreasing strength. In this work, synergistic enhancement of strength and formability is achieved in a Mg-3Al-1Sn-0.5Ca-0.1Sm (ATXS3110) alloy by 0.2 wt.% Mn addition combined with high temperature rolling, exhibiting a high index Erichsen (I.E.) value of ~8.1 mm and near-isotropic mechanical properties. On one hand, after Mn addition, the grain refinement from ~7.6 μm to ~4.1 μm results in suppression of extension twinning, thereby preventing the development of strong basal texture upon stretch forming. On the other hand, trace Mn addition narrows the grain size distribution and promotes the formation of uniform fine grains, which induces homogeneous deformation during stretch forming. Moreover, grain refinement and high-density nano-sized precipitates caused by trace Mn addition increase the strength. This work may provide insights into designing low-cost Mg-Al-Sn series alloys with superior comprehensive mechanical properties for further structural applications.

Keywords: Mg alloy; Rolling; Texture; Alloying; Formability.

1. Introduction

Due to the low density and high specific strength, Mg alloys are promising automotive structural components to further improve fuel efficiency and reduce CO_2 emissions [1-5]. However, the limited strength and cold formability of Mg alloys have restricted their widespread application in industry [6,7]. Alloying is an effective method to improve the strength and formability of Mg alloys. Due to the high solid solubility of Al element in Mg matrix, Mg-Al series alloys have attracted much attention [8-10]. Sn element can reduce the stacking fault energy of Mg alloys and thus enhances the activity of non-basal slip [11]. Ca element can reduce the c/a ratio value, which can enhance the symmetry of the hcp structure, thus promoting the activation of non-basal slip [12]. Therefore, the incorporation of Ca and Sn into Mg-Al series alloys can effectively enhance the ductility. Moreover, the addition of Ca and Sn to Mg-Al series alloys contributes to form high-density nano-sized CaMgSn phase [13], showing remarkable precipitation strengthening. However, the rolled Mg-Al-Sn-Ca series alloys usually exhibit a strong basal texture that impairs their formability [14], e.g., a low index

* Corresponding authors.
E-mail addresses: jinzz031@nenu.edu.cn (Z.-Z. Jin), minzha@jlu.edu.cn (M. Zha).

https://doi.org/10.1016/j.jma.2024.06.022

Erichsen (I.E.) value of ~4.7 mm for Mg-2Al-0.8Sn-0.5Ca alloy [15].

Microalloying of rare earth (RE) elements is considered as an effective way to weaken texture [16-18]. It has been reported that minor Sm addition brought about many beneficial effects on modifying the microstructure and mechanical properties of Mg-Al series alloys [19-22]. First, Wang et al. [22] reported that trace addition of Sm can refine the eutectic phase during solidification, which will enhance the ductility and formability of Mg-Al series alloys. Moreover, the addition of Sm can significantly weaken the texture. For example, after 0.5 wt.% Sm addition, the Mg-2Zn-0.2Mn alloy possessing weak texture exhibits a high I.E. value of ~6.9 mm [19]. Furthermore, the trace addition of Sm can promote grain refinement [20] and grain boundary segregation [21], thereby increasing the strength and ductility of Mg alloys. In addition to alloying, high temperature rolling has proposed as another effective way in weakening basal texture and improving the formability [23]. Huang et al. [24] investigated the effect of rolling temperature on the texture and formability of AZ31 alloy. With increasing rolling temperature from 450 °C to 525 °C, the texture intensity decreased from ~5.4 mrd to ~2.7 mrd, leading to the increasing I.E. value from ~4.5 mm to ~8.6 mm [24]. Using slipping trace analysis, Bian et al. [23] demonstrated that elevated rolling temperature could promote the activation of $<c + a>$ slip. According to quasi-in-situ annealing experiments, grains containing $<c + a>$ dislocations converted to non-basal oriented grains after static recrystallization, thereby weakening the basal texture.

Although texture weakening can enhance the formability of Mg alloys, it is often accompanied by a reduction in yield strength [25]. It is mainly attributed to the fact that texture weakening reduces the Hall-Petch parameters, thereby decreasing the effect of grain boundary strengthening [26]. By introducing high-density precipitates, high yield strength can be achieved though in the weak basal-textured Mg alloys. Nakata et al. [27] reported that nano-sized Al-Mn phase could enhance strength without affecting formability (I.E. value of ~7.2 mm). Therefore, the addition of Mn element to Mg-Al-Sn-Ca alloys is expected to achieve the synergy of high formability and strength.

Although the nano-sized Al-Mn phase has minor influence on formability, the grain refinement due to its pinning effect on grain boundaries imposes a significant effect on formability. Chino et al. [28] reported that for the strongly textured Mg alloys, e.g., AZ31 alloy, the larger the grain size, the better the formability. This is attributed to the fact that large grain size contributes to the activation of twinning, which favors the deformation in thickness direction. Nakata et al. [29] also reported that for the AM30 alloy with a basal circular texture, the activation of extension twins could induce significant texture weakening during stretch forming, thus enhancing the formability. However, Huang et al. reported that reducing the grain size can inhibit twinning and thus enhance the formability of AZ31 alloy with weak basal texture [30]. The effect of grain size on formability is controversial and needs to be further explored.

In this work, we applied the high temperature rolling on Mg-3Al-1Sn-0.5Ca-0.1Sm (ATXS3110) and Mg-3Al-1Sn-0.5Ca-0.2Mn-0.1Sm (ATXS3110-0.2Mn) alloys. The effect of Mn microalloying on microstructural and texture evolution and hence the strength, ductility and formability of ATXS3110 alloy processed by high temperature rolling were systematically investigated. By interrupted Erichsen cupping tests, the influence of grain size on twins and hence the formability of Mg alloys with weak basal texture has been revealed. This work may provide insights into the design of Mg-Al-Sn series alloys with excellent formability.

2. Experimental procedure

The present alloys with nominal compositions of Mg-3Al-1Sn-0.5Ca-0.1Sm (ATXS3110) and Mg-3Al-1Sn-0.5Ca-0.2Mn-0.1Sm (ATXS3110-0.2Mn) were prepared from pure Mg (99.9 wt.%), pure Al (99.9 wt.%), pure Sn (99.9 wt.%), Mg-Ca, Mg-Mn and Mg-Sm master alloys. The pure metals and master alloys were melted in a resistance furnace under protective gas. Then, the purified melt was poured into a copper mould with circulating water to achieve sub-rapid solidification with a high cooling rate of ~150 K/s [31,32]. The size of the copper mould cavity was 80 mm × 50 mm × 5 mm in length, width and thickness, respectively. The measured compositions of the alloys are shown in Table 1.

Fig. 1 shows the schematic diagram of the thermal processing history of ATXS3110 and ATXS3110-0.2Mn alloys. The cast plates were homogenized at 420 °C for 2 h and 480 °C for 3 h in a tube furnace under protective gas followed by water quenching. Before rolling, the rollers were heated to 100 °C. Then as-homogenized plates were rolled for 4 passes at 450 °C with the total thickness reduction of ~80%. The plates were held at 450 °C for 10 min before each pass, and the rolling direction was rotated by 90° clockwise relative to the previous pass. The rolling direction of the last pass was defined as rolling direction (RD). The rolled plates were annealed at 450 °C for 1 h to obtain fully recrystallized

Table 1
Measured compositions of ATXS3110 and ATXS3110-0.2Mn alloys.

Nominal compositions	Measured compositions (wt.%)					
	Al	Sn	Ca	Mn	Sm	Mg
Mg-3Al-1Sn-0.5Ca-0.1Sm	2.76	1.20	0.59	—	0.12	Bal.
Mg-3Al-1Sn-0.5Ca-0.2Mn-0.1Sm	2.72	1.24	0.59	0.24	0.14	Bal.

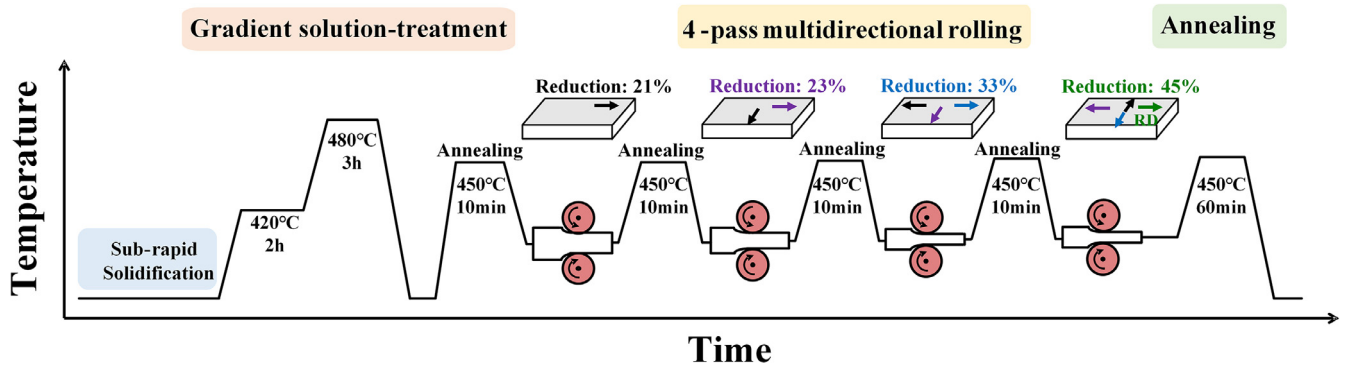

Fig. 1. The schematic illustration for thermo-mechanical history of ATXS3110 and ATXS3110-0.2Mn alloys.

structure. For comparison, samples rolled and annealed at 350 °C with the same method were also prepared.

Room temperature tensile testing was carried out on an electric universal testing machine (AGS-X-100KN) under a strain rate of 1×10^{-3} s^{-1}. The tensile samples were dog-bone shaped with a gauge size of 10 mm, 4 mm, and 1 mm in length, width, and thickness, respectively. The tensile samples were cut from the annealed plates with the tensile direction parallel to RD, 45° to RD (denoted as 45°), and transverse direction (TD), respectively to calculate the Lankford value (r-value). The calculation formula is as follows:

$$r = \varepsilon_w/\varepsilon_t \tag{1}$$

where ε_w and ε_t are the stain along width and thickness, respectively. To ensure that the data were under uniform deformation conditions, a tensile strain of 0.1 was used to calculate the r value. To evaluate the plastic anisotropy, the average r-value (r_{avg}) and in-plane anisotropy (Δr) were also calculated by tension along different directions [33]. The formulas for these calculations are as follows:

$$r_{avg} = \frac{1}{4}(r_{RD} + 2r_{45} + r_{TD}) \tag{2}$$

$$\Delta r = \frac{1}{2}(r_{RD} + r_{TD} - 2r_{45}) \tag{3}$$

To assess the room-temperature formability, Erichsen cupping tests were conducted using samples with a diameter of 50 mm. The punch diameter was 20 mm, and the punch speed was set to 0.1 mm/s. At least three samples were tested for each tensile test and Erichsen cupping test to ensure reproducibility.

Coarse eutectic phases, deformation twins and texture were analyzed by a field emission scanning electron microscope (SEM, Sigma 500) equipped with an energy dispersive spectrometer (EDS) and an electron backscattered diffraction detector (EBSD, Oxford Instruments Symmetry). EBSD data were processed and analyzed using channel 5 software. Dislocation types, nano-sized precipitates and grain boundary segregation were characterized by transmission electron microscopy (TEM, Talos F200X). Thin foils for TEM characterization were processed by mechanical milling to ~80 μm, and then twin-jet electropolishing for perforation and ion-milling at −150 °C by the Gatan 691 Precision Ion Polishing System.

3. Results

3.1. Mechanical properties

Fig. 2(a) and (b) show the room-temperature tensile stress-strain curves along the RD, 45° and TD, and Erichsen cupping results of annealed ATXS3110 and ATXS3110-0.2Mn alloys. It can be seen that both alloys display almost overlapped tensile curves along different directions, indicating an excellent tensile mechanical isotropy. The yield strength (YS), ultimate tensile strength (UTS), elongation to fracture (EF) and index Erichsen (I.E.) value are summarized in Table 2. Notably, the I.E. value significantly increases from ~5.4 mm to ~8.1 mm after trace Mn addition. Meanwhile, the average YS, UTS and EF increase by ~10 MPa, ~9 MPa and ~4%, respectively. It breaks through the general idea that strength and formability are trade-off and difficult to enhance simultaneously. Fig. 2(c) and (d) compare the YS, EF and I.E. values of Mg-Al and Mg-Zn-RE series alloys in literature [34-50]. Owing to the trade-off dilemma between strength and formability, the relationship between I.E. value and YS usually shows banana-shaped curve as illustrated by two dotted lines. One can see that the present ATXS3110-0.2Mn alloy located at the upper-right corner in Fig. 2(c) and (d), indicating a great combination of formability, yield strength and ductility, which is superior to most previously reported Mg-Al and Mg-Zn-RE series alloys.

Lankford value (r-value) and strain-hardening exponent (n-value) could reflect the formability of Mg alloys. A larger n value corresponds to better UE and formability [38]. While a smaller r_{avg} is favorable for deformation of plate along the thickness direction [51]. The Δr value represents the planar anisotropy of the plates [33], i.e., a large Δr value implies severe anisotropy and poor stretch formability capacity. From Table 2, one can see that both alloys have comparable average n-values, i.e., ~0.247 for Mn-free alloy and ~0.25 for Mn-containing alloy, which coincides with the trend of

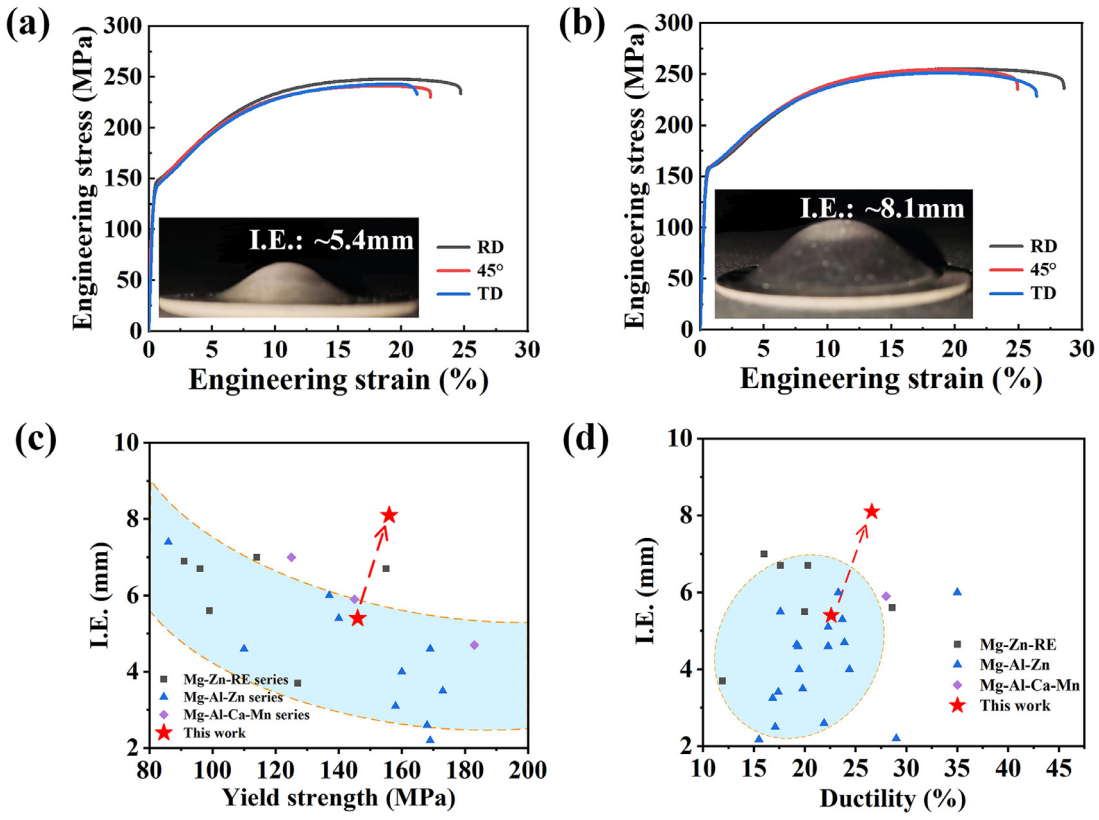

Fig. 2. Tensile engineering stress-strain curves with tension directions parallel to RD, 45° and TD, as well as Erichsen cupping test results of the annealed (a) ATXS3110 and (b) ATXS3110-0.2Mn alloys; (c, d) average YS *vs.* I.E. values and average ductility *vs.* I.E. values for the present alloys and Mg-Al and Mg-Zn-RE series alloys in literature [34-50].

average UE, i.e., ~18.8% for Mn-free alloy and ~19.6% for Mn-containing alloy. However, Mn-containing alloy exhibits smaller r_{avg} and Δr values compared to Mn-free alloy, indicating better isotropy and deformation ability along the thickness direction.

3.2. The evolution of microstructure and texture

As-rolled ATXS3110 and ATXS3110-0.2Mn alloys were characterized by EBSD as shown in Fig. 3. Both as-rolled alloys contain deformed grains with high-density dislocations and a few twins (Fig. 3(a-c) and (e-g)). In addition, there are almost no shear bands in both alloys. From the inserted images in Fig. 3(a) and (e), both as-rolled alloys show strong basal texture with the texture intensity of ~12.2 mrd for Mn-free alloy and ~11.3 mrd for Mn-containing alloy. The area fraction of dynamic recrystallized grains after the fourth pass of rolling is ~8.7% for Mn-free alloy and ~4.9% for Mn-containing alloy (Fig. 3(d) and (h)). This implies that the addition of Mn inhibits dynamic recrystallization, which is attributed to the increasing number of nano-sized phases [52].

Fig. 4 illustrates EBSD inverse pole figure (IPF) maps, grain size distribution and texture of annealed ATXS3110 and ATXS3110-0.2Mn alloys. After annealing, both alloys exhibit fully recrystallized grain structures (Fig. 4(a) and (d)). Trace Mn addition results in the remarkable grain refinement with decreasing average grain size from ~7.6 μm to ~4.1 μm (Fig. 4(b) and (e)). Moreover, the grain size distribution becomes narrower and the relative frequency of grains larger than 10 μm decreases from ~11.9% to ~1.3%. From

Table 2
Tensile properties, n values, Lankford values (r-value), r_{avg}, Δr and Index Erichsen values of annealed ATXS3110 and ATXS3110-0.2Mn alloys.

Alloy		YS (MPa)	UTS (MPa)	EF (%)	n-value	r-value	r_{avg}	Δr	I.E. (mm)
ATXS3110	RD	146.3 ± 2.8	248.0 ± 3.4	24.6 ± 0.7	0.25	1.37	1.39	0.30	5.4 ± 0.6
	45°	141.4 ± 2.2	241.4 ± 1.8	22.3 ± 1.4	0.24	1.54			
	TD	140.7 ± 2.7	243.0 ± 3.6	21.0 ± 1.9	0.25	1.10			
ATXS3110-0.2Mn	RD	158.1 ± 3.2	255.5 ± 2.4	28.6 ± 1.4	0.26	1.43	1.17	0.08	8.1 ± 0.3
	45°	154.9 ± 1.9	254.7 ± 2.7	25.0 ± 1.9	0.25	1.13			
	TD	155.2 ± 2.6	251.7 ± 3.9	26.4 ± 1.8	0.24	1.00			

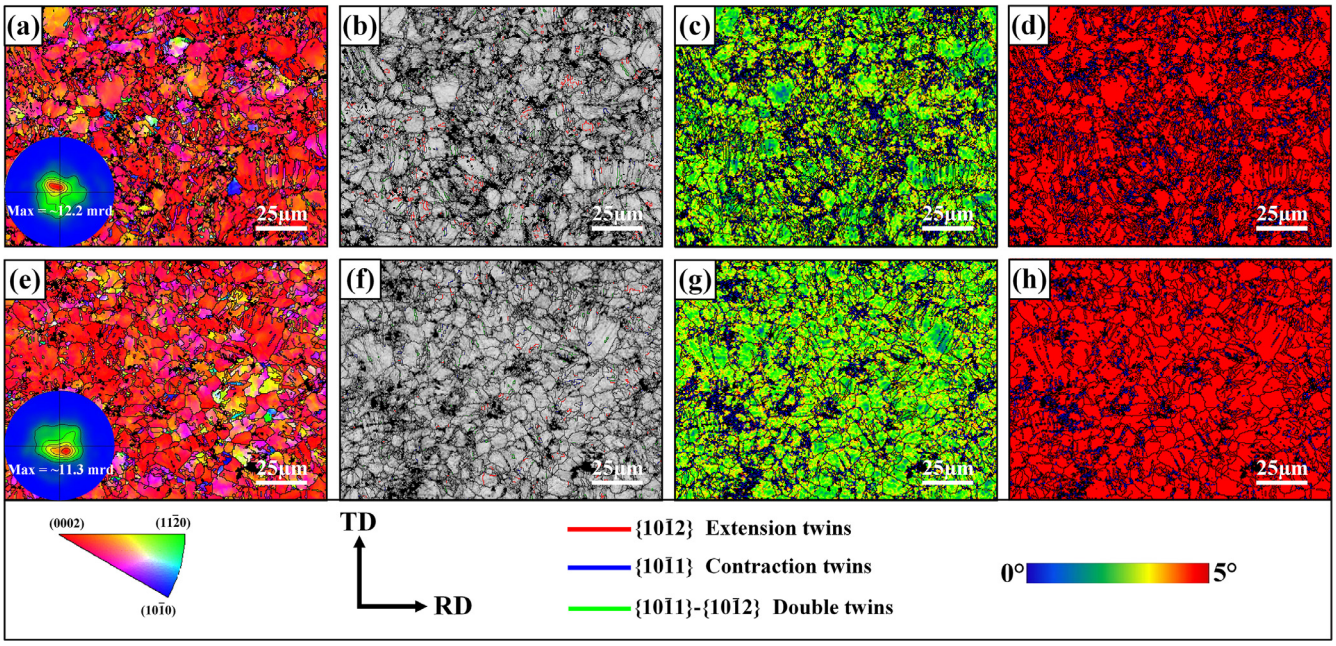

Fig. 3. EBSD inverse pole figure (IPF) maps (inserted images are corresponding (0002) pole figures), band contrast maps, kernel average misorientation (KAM) maps and distribution of recrystallized and deformed grains (where red represents deformed grains, blue represents recrystallized grains) of as-rolled (a-d) ATXS3110 and (e-h) ATXS3110-0.2Mn alloys; extension twins, contraction twins and double twins are highlighted by red, blue and green lines in (b) and (f), respectively.

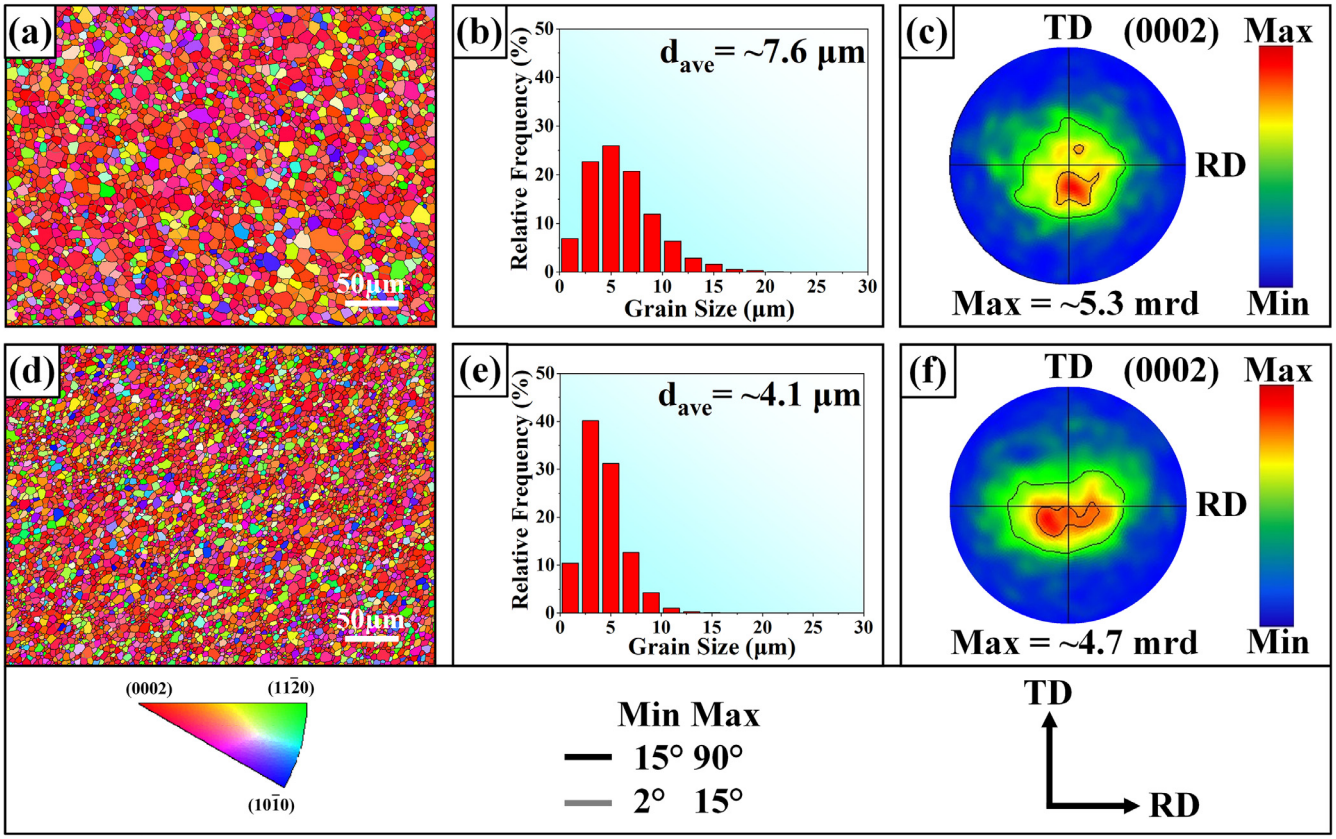

Fig. 4. EBSD inverse pole figure (IPF) maps, grain size distributions maps and (0002) pole figures of annealed (a-c) ATXS3110 and (d-f) ATXS3110-0.2Mn alloys.

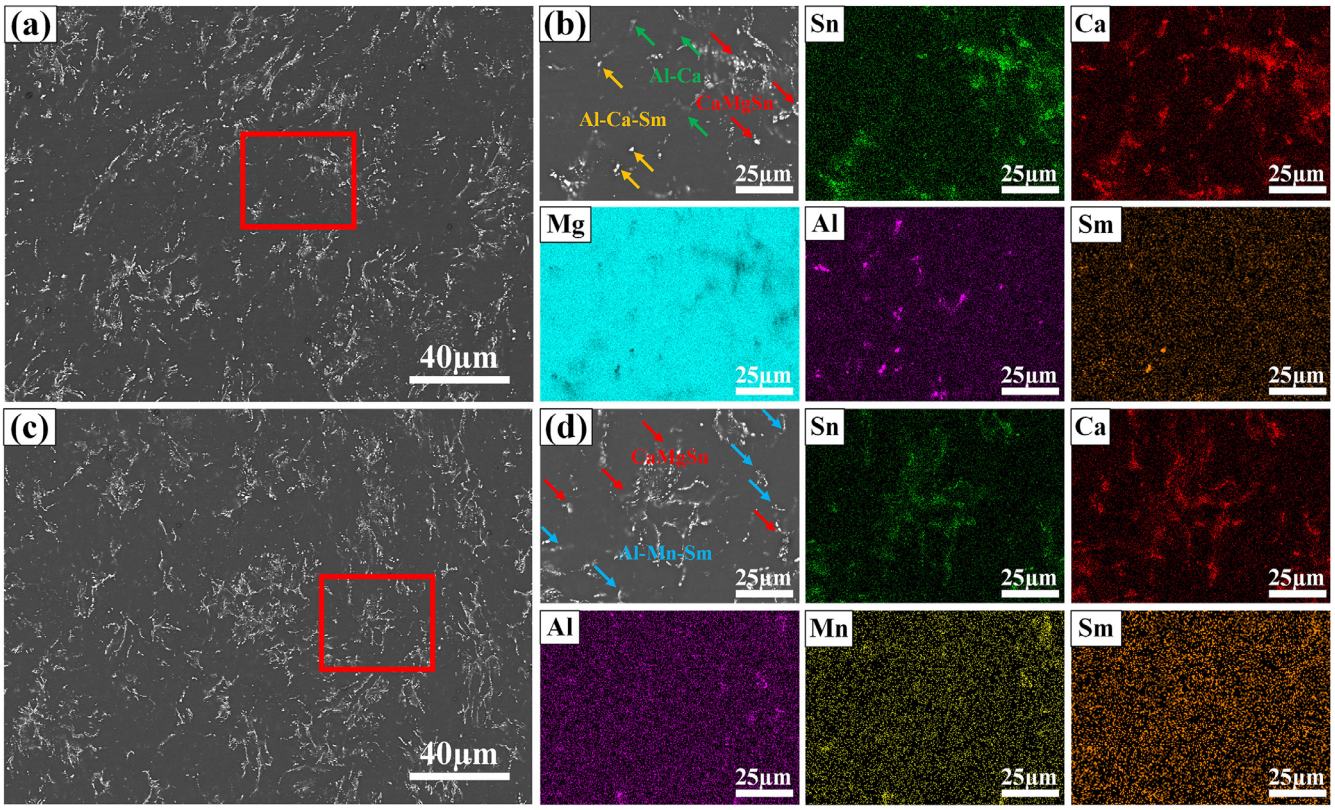

Fig. 5. (a, c) Backscattered electron (BSE) images and (b, d) the corresponding energy dispersive spectrometer (EDS) analysis of annealed (a, b) ATXS3110 and (c, d) ATXS3110-0.2Mn alloys.

Fig. 4(c) and (f), both ATXS3110 and ATXS3110-0.2Mn alloys exhibit RD-split weak basal texture with the texture intensity of ~5.3 mrd and ~4.7 mrd, respectively. It is noteworthy that the texture intensity of Mn-containing alloy in both rolled and annealed states is lower than that of Mn-free alloy, suggesting that Mn element could promote the weakening of texture. The addition of Mn to weaken the texture has been reported in Mg-Er [53], Mg-Gd [54] and Mg-Mn-Al alloys [55]. It was attributed to the fact that the addition of Mn could narrow the CRSS gap between non-basal and basal slip, thus promoting the activation of non-basal dislocations during rolling and annealing, leading to the weakening of texture [53].

Fig. 5(a-d) show the backscattered electron (BSE) images and EDS mappings of annealed ATXS3110 and ATXS3110-0.2Mn alloys. As shown in Fig. 5(a) and (c), both annealed alloys contain a large number of feathery-shaped phases, which are identified as CaMgSn phase according to EDS mapping (Fig. 5(b) and (d)). After multiple-pass rolling, CaMgSn phase has been fragmented into spherical particles with a few micrometers (as indicated by red arrows in Fig. 5(b) and (d)). In addition, the annealed Mn-free alloy contains numerous spherical Al-Ca phases (as indicated by green arrows in Fig. 5(b)) and a few spherical Al-Ca-Sm phases (as indicated by yellow arrows in Fig. 5(b)). With the addition of Mn element, a few Al-Mn-Sm phases are formed (as indicated by blue arrows in Fig. 5(d)), while Al-Ca and Al-Ca-Sm phases almost disappear. The area fraction of second phases in annealed Mn-free and Mn-containing alloys is ~7.6% and ~7.2%, respectively.

Fig. 6 shows the phase diagram of Mg-3Al-1Sn-0.5Ca-0.1Sm-xMn (x = 0–0.4) alloy and phase fraction of Mn-free and Mn-containing alloys calculated by Pandat software. According to the Fig. 6(b), the Al-Ca phase in the Mn-free alloy is inferred as Al_4Ca phase, while the Al-Ca-Sm phase is identified as the Al_3Sm phase with a small amount of Ca dissolved in it. For the Mn-containing alloy, the Al-Mn-Sm phase is inferred as Al_8Mn_4Sm phase (Fig. 6(c)). Moreover, the phase diagram indicates that both Mn-free and Mn-containing alloys contain numerous $Mg_{17}Al_{12}$ phase, though $Mg_{17}Al_{12}$ phase can be rarely found in BSE figures for both alloys (Fig. 5(a-d)). It is attributed to that the high cooling rate induced by SRS may change the solidification paths [13].

To identify the feature and type of nano-sized phases, detailed high-angle annular dark-field scanning transmission electron microscopy (HAADF-STEM) and high-resolution TEM (HR-TEM) images of annealed ATXS3110 and ATXS3110-0.2Mn alloys are presented in Figs. 7 and 8. According to the EDS mapping (Fig. 7(c)), the annealed Mn-free alloy contains two types of spherical phases. One composes of Al and Ca elements, and the other contains Ca and Sn elements. Combined with HR-TEM, they can be identified as Al_2Ca and CaMgSn phases (Fig. 7(d-g)). It is noteworthy that abundant Sm solutes enrich within Al_2Ca phase for

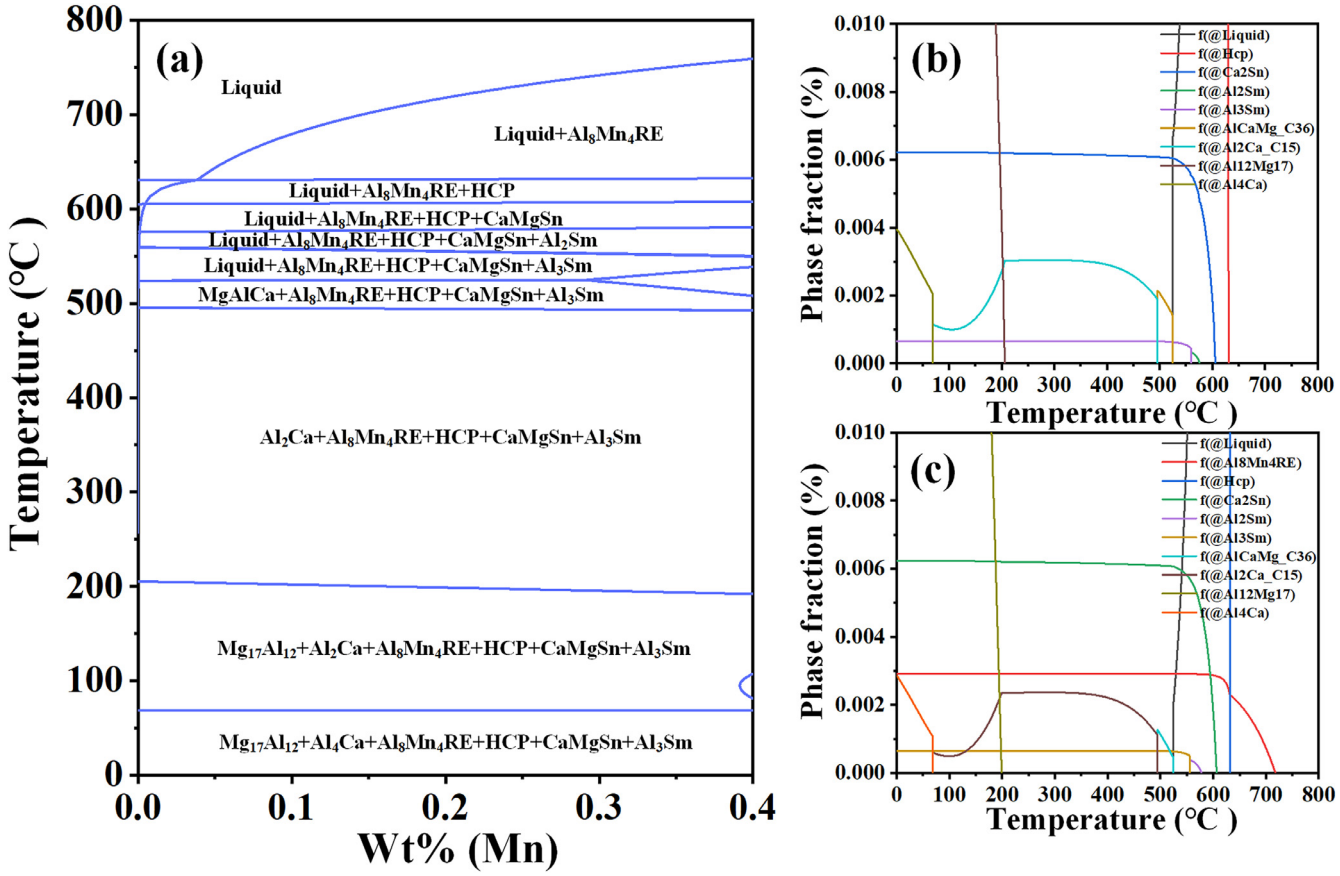

Fig. 6. (a) Phase diagram of Mg-3Al-1Sn-0.5Ca-0.1Sm-xMn alloy (x = 0–0.4), phase fraction as a function of temperature for (b) Mg-3Al-1Sn-0.5Ca-0.1Sm and (c) Mg-3Al-1Sn-0.5Ca-0.1Sm-0.2Mn alloys.

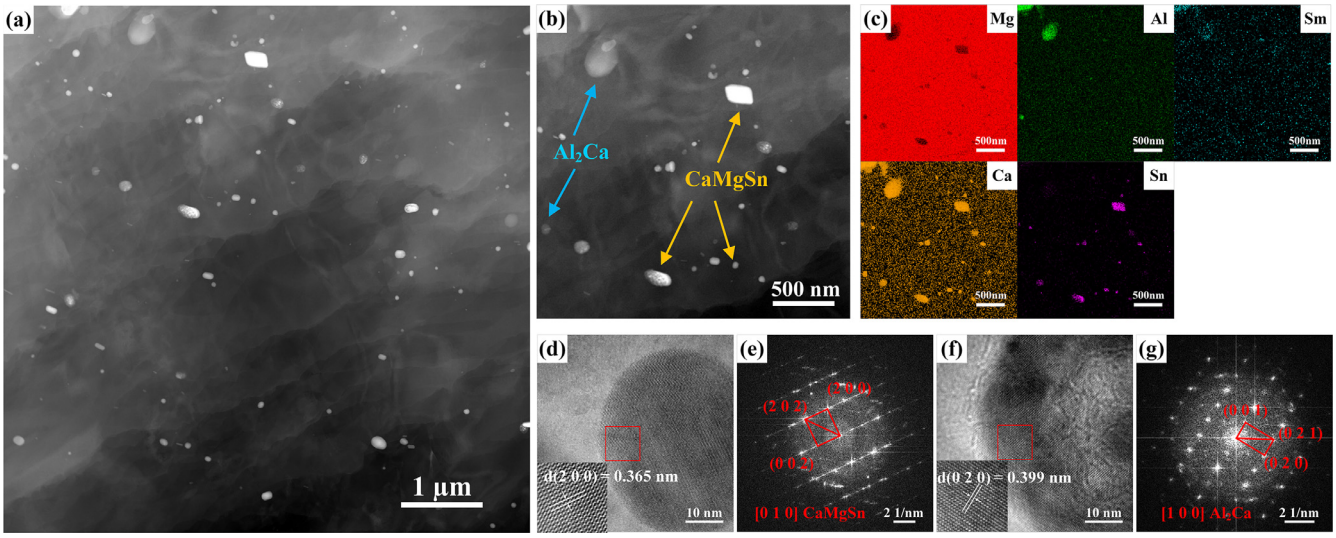

Fig. 7. (a, b) HAADF-STEM image and (d, f) HR-TEM (the inset is an enlargement of the red box region) of typical nano-sized phases in annealed ATXS3110 alloy, (c) corresponding EDS maps of (b), (e, g) corresponding fast flourier transform of (d, f).

Mn-free alloy (Fig. 7(c)), resulting from the large electronegativity difference between Sm and Al elements [56]. With the addition of Mn, the Al_2Ca phase disappears (Fig. 8(b) and (c)). Instead, both rod-like and spherical Al-Mn-Ca phases appear, which are identified as Al_8Mn_4Ca phases based on HR-TEM (Fig. 8(d) and (e)). According to the low magnified images (Fig. 7(a) and Fig. 8(a)), the trace Mn addition could effectively promote the precipitation of nano-sized phases.

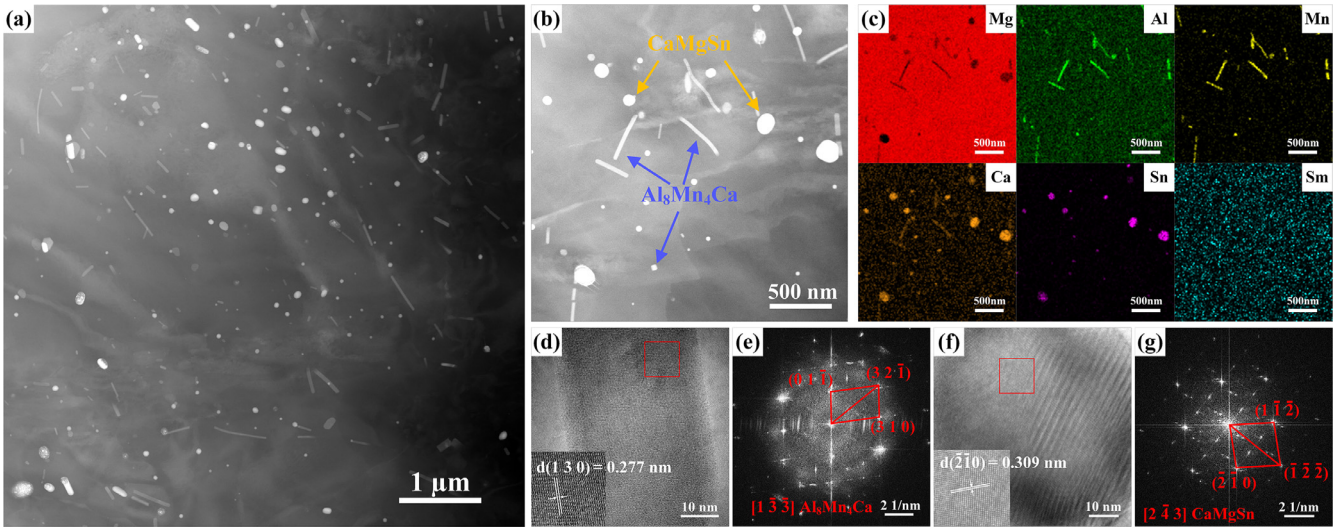

Fig. 8. (a, b) HAADF-STEM image and (d, f) HR-TEM (the inset is an enlargement of the red box region in the figure) of typical nano-sized phases in annealed ATXS3110-0.2Mn alloy, (c) corresponding EDS maps of (b), (e, g) corresponding fast flourier transform of (d, f).

Table 3
The ratio of extension, contraction and double twin boundaries to total grain boundaries at different positions in annealed ATXS3110 and ATXS3110-0.2Mn alloys after interrupted Erichsen cupping test with the punch stroke of 2 mm.

Alloy		Extension twin (%)	Contraction twin (%)	Double twin (%)	Total (%)
ATXS3110	Top half	3.4	0.3	1.1	3.8
	Bottom half	25.1	0.2	0.1	25.4
ATXS3110-0.2Mn	Top half	2.2	0.2	0.2	2.6
	Bottom half	3.1	0.3	0.2	3.6

The number density of nano-sized phases in the ATXS3110-0.2Mn alloy is higher than that in the ATXS3110 alloy, i.e., 1.6×10^{20} m^{-3} vs. 5.1×10^{19} m^{-3}.

3.3. Microstructure evolution during Erichsen cupping test

To investigate the origin of the significant difference in I.E. values between annealed ATXS3110 and ATXS3110-0.2Mn alloys, interrupted Erichsen cupping tests and corresponding EBSD characterizations were performed. Fig. 9 displays the EBSD maps for both alloys with a punch stroke of 2 mm. Note that a large number of low angle grain boundaries (LAGBs) exist in the top half of both plates (Fig. 9(a-d)). This position possesses a higher kernel average misorientation (KAM) value (Fig. 9(e-h)) compared with the bottom half region. It indicates that the strain in the top half is much higher than that in the bottom half, which is consistent with the results in literature [15]. From Fig. 9(i-l), extension twin is the dominant twin type at different locations in both alloys. However, the number of extension twins in the bottom half is quite distinguished in two alloys. In the bottom half of Mn-free alloy, extension twinning occurs in 29% of the grains (in terms of number fraction). In comparison, about 11% of grains exhibit extension twinning in the bottom half of Mn-containing alloy. Table 3 summarizes the fraction of different types of twin boundaries to total grain boundaries at different positions after the interrupted Erichsen cupping test with the punch stroke of 2 mm. It is evident that the twin fraction rarely changes in the top half after Mn addition. However, in the bottom half, the fraction of extension twins boundaries to total grain boundaries in the Mn-free alloy (~25.1%) is much higher than that in the Mn-containing alloy (~3.1%). The remarkable difference in twinning activity is closely related to grain size, as twins can be more easily formed in large grains over 10 μm during room-temperature deformation [57]. Thereby, numerous twins are prone to be formed during stretch forming in the Mn-free alloy containing more grains larger than 10 μm (Fig. 4(b)).

Fig. 10 shows the EBSD results of both ATXS3110 and ATXS3110-0.2Mn alloys after the interrupted Erichsen cupping test with a punch stroke of 5 mm. From the IPF maps (Fig. 10(a-d)), a significant number of low angle grain boundaries (LAGBs) are formed in both alloys. For Mn-free alloy, the number of LAGBs in coarse grains is considerably lower than that in fine grains (Fig. 10(a) and (b)). It was reported that LAGBs can emit dislocations and enhance the dislocation multiplication ability, which contribute to coordinate deformation [58,59]. The lower density of LAGBs in coarse grains limits their ability to coordinate deformation. According to KAM maps (Fig. 10(e) and (f)), the KAM values inside

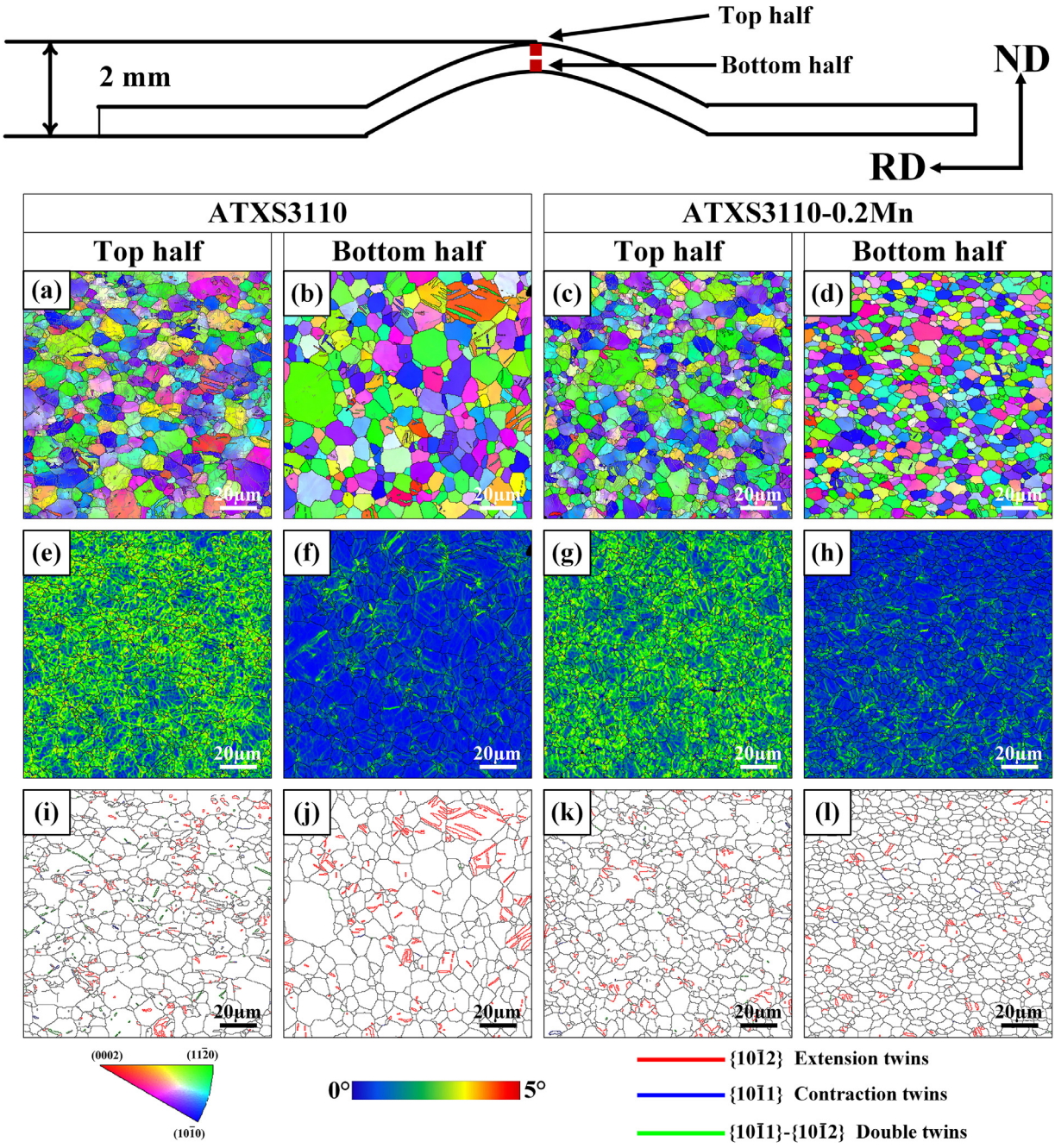

Fig. 9. (a-d) EBSD-IPF, (e-h) KAM and (i-l) twin boundary maps of annealed ATXS3110 and ATXS3110-0.2Mn alloys after interrupted Erichsen cupping test with the punch stroke of 2 mm.

coarse grains are lower than those of fine grains, implying that these coarse grains are difficult to deform. Owing to the incompatible deformation among coarse grains and fine grains, plastic strain localization spreads into grain boundaries and the grain interior, leading to stress concentration. Upon further deformation, the localized plastic deformation is prone to induce microcracks, resulting in early fracture of the Mn-free alloy. In contrast, the uniform distribution of KAM in the Mn-containing alloy indicates more uniform deformation upon stretch forming (Fig. 10(g) and (h)).

Due to the occurrence of de-twinning, the number of twins in both ATXS3110 and ATXS3110-0.2Mn alloys significantly decreases with increasing punch stroke from 2 mm to 5 mm. However, many elongated double twins with high strains (as marked by blue arrows in Fig. 10(i) and (j)) can be observed in coarse grains for the Mn-free alloy, leading to the formation of microcracks. By contrast, almost no double twins can be observed in the ATXS3110-0.2Mn alloy (Fig. 10(k) and (l)).

Fig. 11 shows the evolution of texture during stretch forming for both ATXS3110 and ATXS3110-0.2Mn alloys. Com-

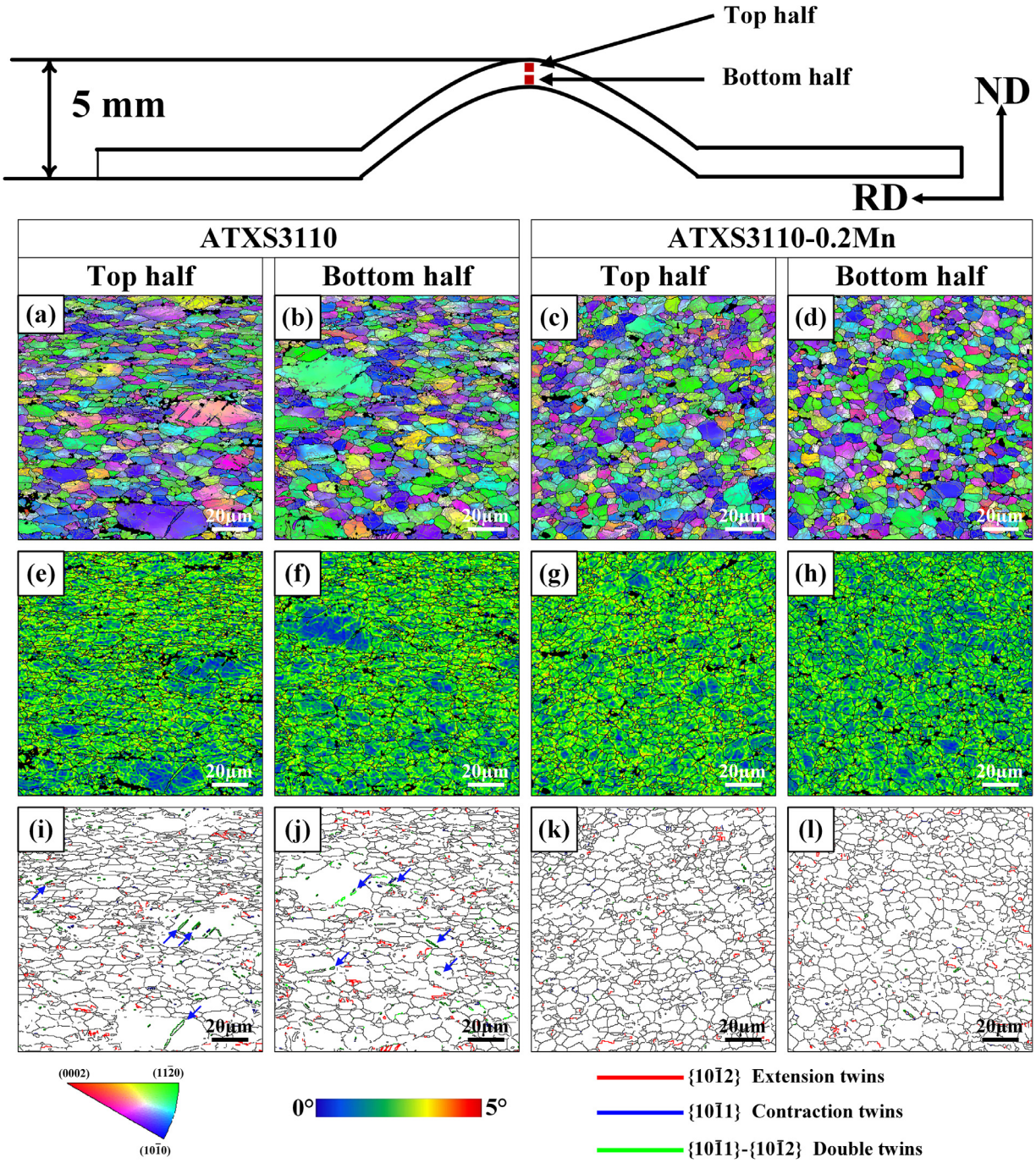

Fig. 10. (a-d) EBSD-IPF, (e-h) KAM and (i-l) twin boundary maps of annealed ATXS3110 and ATXS3110-0.2Mn alloys after interrupted Erichsen cupping test with the punch stroke of 5 mm.

pared with annealed state (~5.3 mrd), with a punch stroke of 2 mm, the texture intensity of the Mn-free alloy significantly increases to ~8.8 mrd and ~13.3 mrd for top half and bottom half, respectively (Fig. 11(a) and (e)). When the punch stroke increases to 5 mm, the texture intensity of the Mn-free alloy decreases to ~7.5 mrd and ~8.1 mrd in top half and bottom half, respectively (Fig. 11(b) and (f)). Differently, in the bottom half of the ATXS3110-0.2Mn alloy, compared to the texture intensity with a punch stroke of 2 mm (~3.7 mrd), the texture intensity significantly increases to ~5.3 mrd with a punch stroke of 5 mm (Fig. 11(g) and (h)). Similar observation was also found in the top half, from ~5.5 to ~6.3 mrd (Fig. 11(c) and (d)). It is attributed to the fact that basal slip remains the dominant deformation mechanism during stretch forming [50], and the activation of a large amount of basal slip leads to an increase in the texture intensity and a transition of the texture type to basal texture [60].

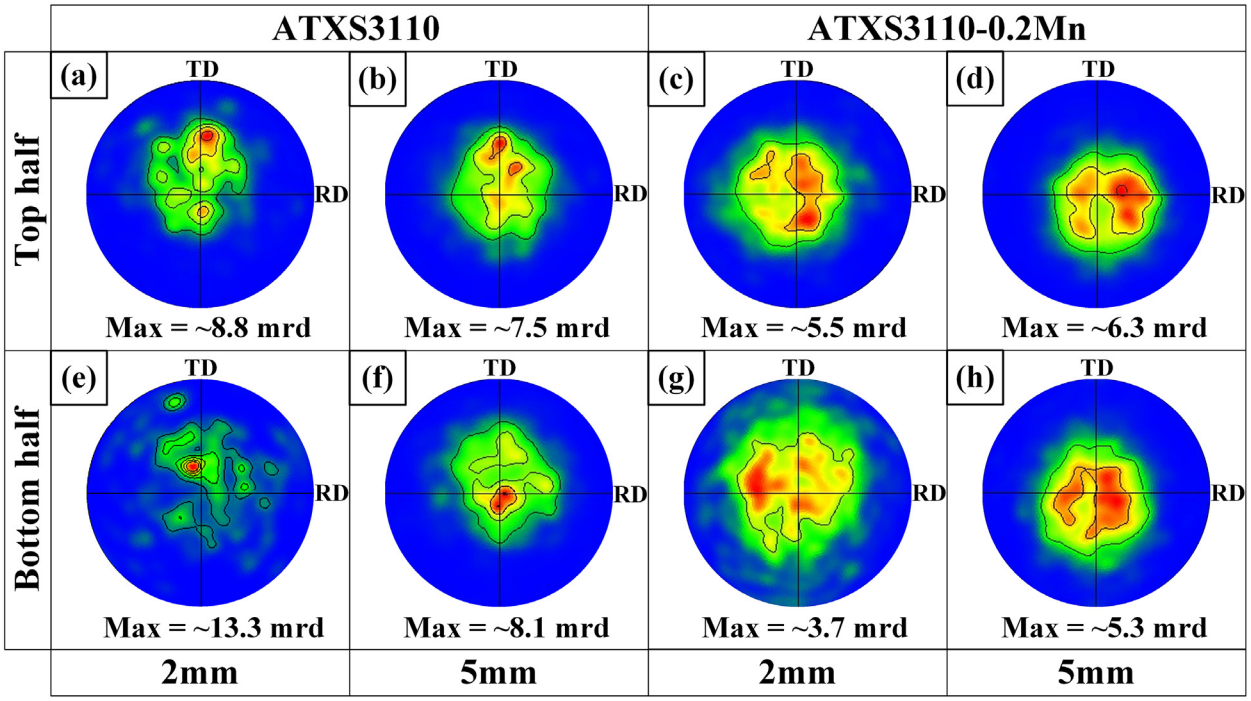

Fig. 11. (0002) pole figure of annealed (a, b, e, f) ATXS3110 and (c, d, g, h) ATXS3110-0.2Mn alloys after interrupted Erichsen cupping test (punch stroke: 2 mm and 5 mm).

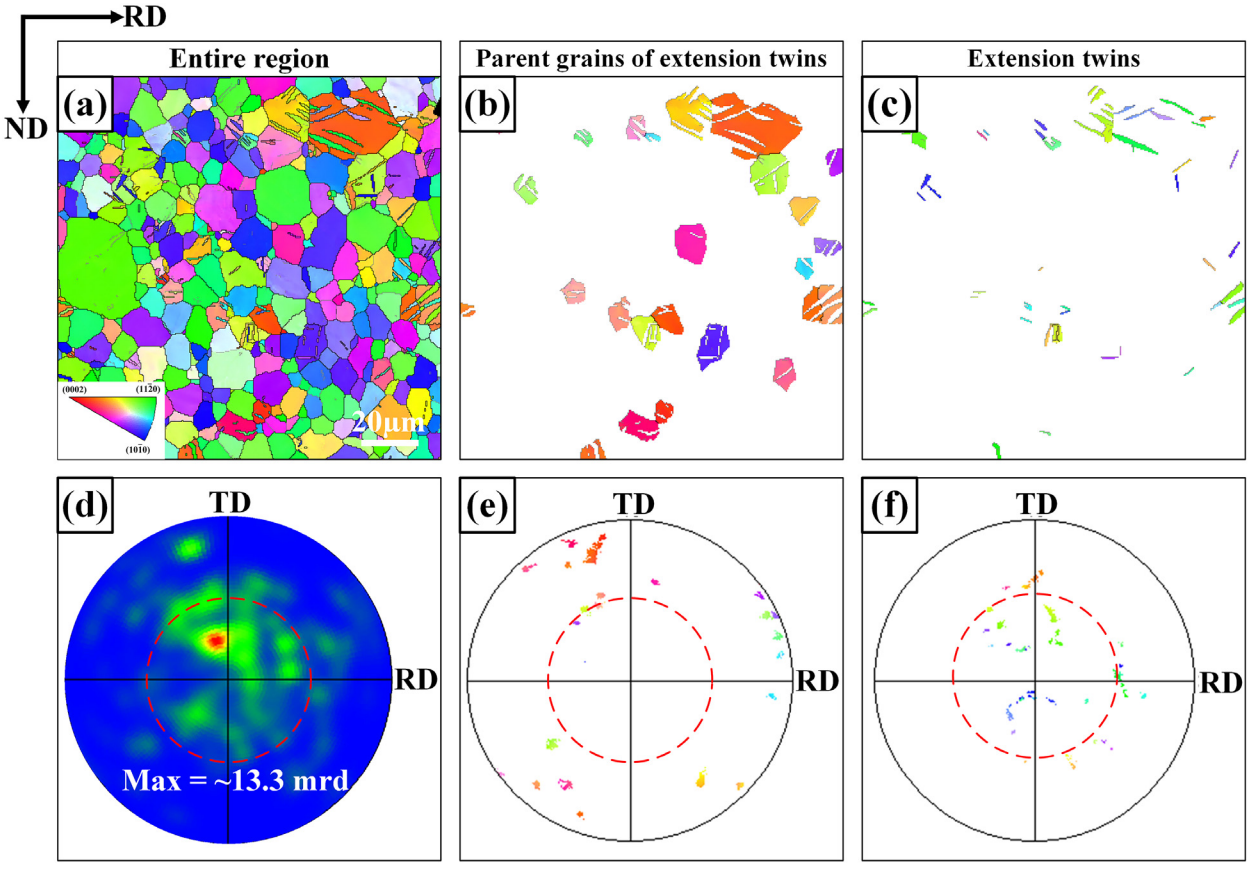

Fig. 12. (a-c) IPF and (d-f) (0002) pole figures showing the orientation of extension twins and their parent grains in bottom half of ATXS3110 alloy with a punch stroke of 2 mm.

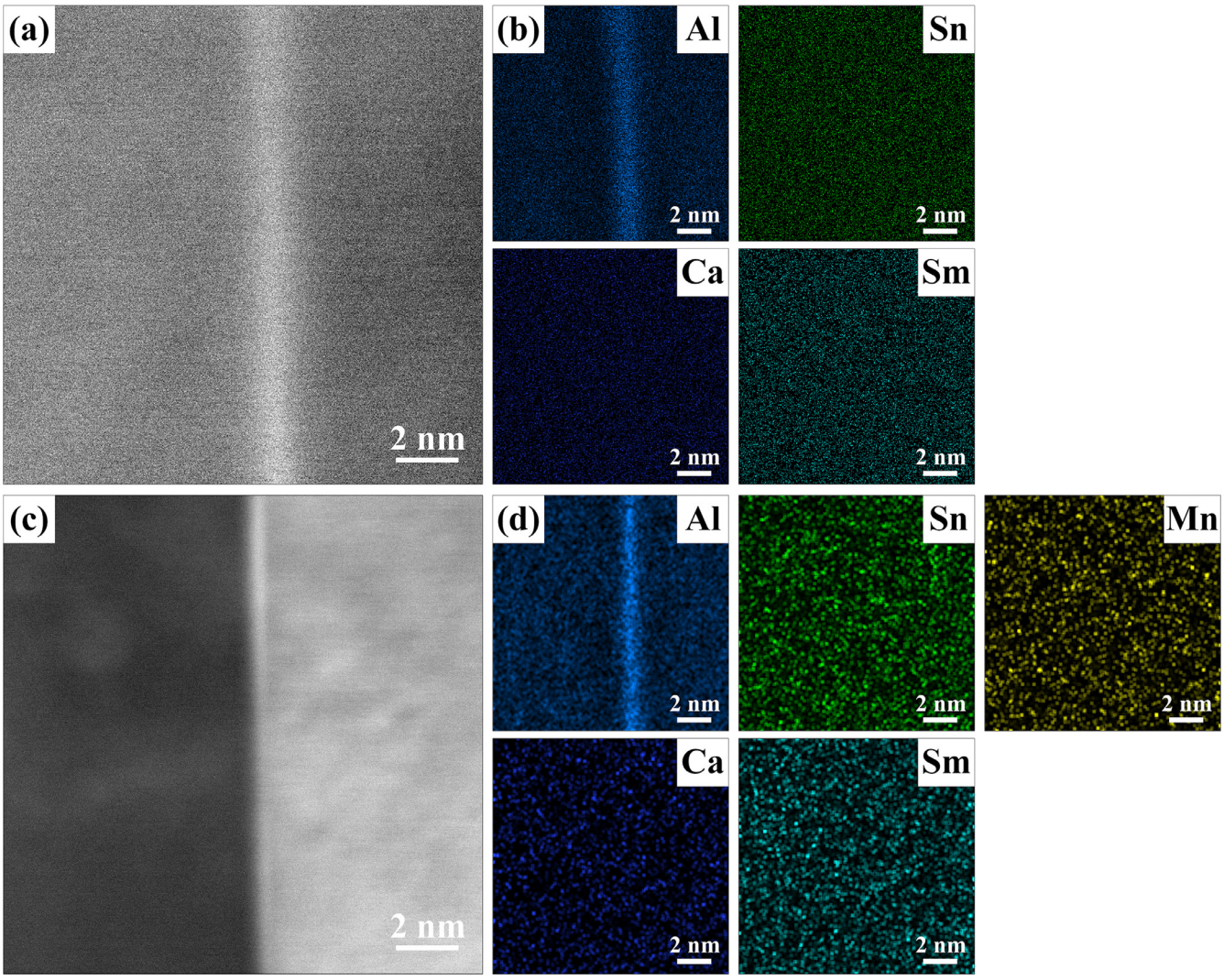

Fig. 13. (a, c) HAADF-STEM and (b, d) EDS maps of annealed (a, b) ATXS3110 and (c, d) ATXS3110-0.2Mn alloys.

The difference in texture evolution is mainly attributed to the activity of twinning. When the punch stroke is 2 mm, the fraction of extension twins boundaries to total grain boundaries at the top and bottom half in Mn-free alloy is ~3.4% and ~25.1%, respectively (Fig. 9(i) and (j)). Fig. 12 shows the IPF and pole figure of extension twins and their parent grains for the bottom half of Mn-free alloy at a punch stroke of 2 mm. We define the grains with angle between the c-axis and ND less than 45° as near-basal oriented grains and greater than 45° as non-basal oriented grains. The red circle in Fig. 12(d-f) represents the dividing line between non-basal and near-basal oriented grains. Note that most of parent grains in Mn-free alloy show non-basal orientation (Fig. 12(b) and (e)), while extension twins exhibit near-basal orientation (Fig. 12(c) and (f)). Therefore, it can be concluded that extension twins contribute to the formation of basal texture in Mn-free alloy at the early stage of stretch forming.

When the punch stroke reaches 5 mm, de-twinning occurs, resulting in the decreasing texture intensity of Mn-free alloy. However, the fraction of extension twins boundaries to total grain boundaries at the top and bottom half in Mn-containing alloy with the punch stroke of 2 mm is as low as ~2.2% and ~3.1% (Fig. 9(k) and (l)), respectively, leading to the limited variation of texture intensity. Concerning the smaller grain size of Mn-containing alloy, the nucleation and growth of twins is suppressed, while multiple slip modes can be activated to coordinate deformation [57,61].

4. Discussion

4.1. The mechanisms for the formation of weak basal texture

Texture imposes a significant influence on formability [23]. Strongly textured Mg alloys usually possess the limited deformability along thickness direction that restricts their formability. In the present work, annealed ATXS3110-0.2Mn alloy exhibits a weak basal texture (Fig. 4(f)), which is necessary for achieving the high formability. Therefore, it is worthwhile

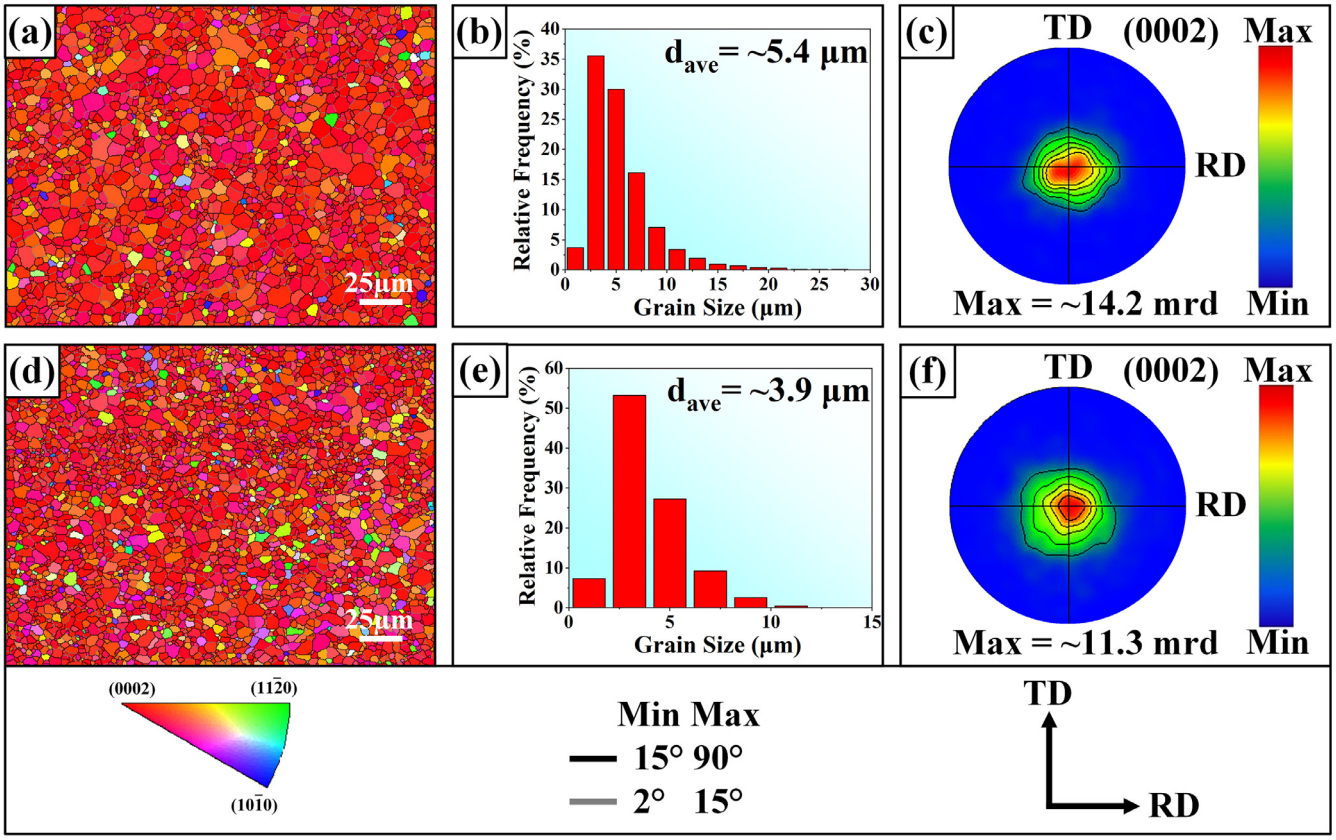

Fig. 14. EBSD inverse pole figure (IPF) maps, grain size distributions maps and (0002) pole figures of annealed (a-c) ATXS3110 and (d-f) ATXS3110-0.2Mn alloys at rolling and annealing temperature of 350 °C.

to investigate the reason for the texture weakening during annealing.

Various mechanisms could explain the weakening of texture in Mg alloys during annealing, such as particle stimulated nucleation (PSN) [62], deformation twin induced nucleation (DTIN) [63,64], shear band induced nucleation (SBIN) [65], etc. The PSN mechanism demonstrates that second phase particles larger than 1 μm can provide the nucleation sites for recrystallized grains. In the present work, the average size and area fraction of second phase for annealed Mn-free alloy was ~1.3 μm and ~7.6%, respectively. And that is ~1.2 μm and ~7.2% for annealed Mn-containing alloy. The size and area fraction of second phase for two alloys are comparable, indicating that PSN mechanism is not the main reason for texture weakening in Mn-containing alloy. According to literature [63,66, 67], double twins can induce the weakening of texture. However, the fraction of double twins boundaries to total grain boundaries is ~2.3% and ~1.4% in as-rolled ATXS3110 and ATXS3110-0.2Mn alloys (Fig. 3(g)), respectively. Such limited twin fraction cannot be the main reason for texture weakening. In addition, neither ATXS3110 nor ATXS3110-0.2Mn alloys contain shear bands. Therefore, SBIN is also not the main mechanism for texture weakening.

It is well accepted that solute segregation at grain boundaries can restrict the growth of basal-oriented grains and promote the growth of non-basal oriented grains, thus inducing the weakening of texture [68]. HADDF-STEM and EDS mapping were conducted to investigate the grain boundary segregation of both ATXS3110 and ATXS3110-0.2Mn alloys (Fig. 13(a-d)). Apparently, Al segregation can be observed at grain boundaries in both alloys. However, the individual role of Al segregation can rarely induce such obvious texture weakening. Since the atomic radius of Al is smaller than that of Mg, another element with a larger atomic radius than Mg must be simultaneously segregated along grain boundaries to minimize the elastic strain at grain boundaries, which could produce an effective solute drag effect and inhibit the preferential growth of basal-oriented grains [69]. Thus, grain boundary segregation cannot be responsible for the formation of weak texture in both alloys.

Bian et al. [23] found that higher rolling temperature promoted the activation of $<c + a>$ slip, which accelerated the nucleation and growth of non-basal grains during subsequent annealing, resulting in the formation of a RD-split weak basal texture. In order to verify the role of high temperature rolling in texture weakening, the samples rolled and annealed at lower temperature (350 °C) with the same processing and annealing treatment were prepared for comparison. Fig. 14 shows the EBSD results after rolling and annealing at lower temperatures (350 °C). Both ATXS3110 and ATXS3110-0.2Mn alloys exhibit a stronger basal texture with

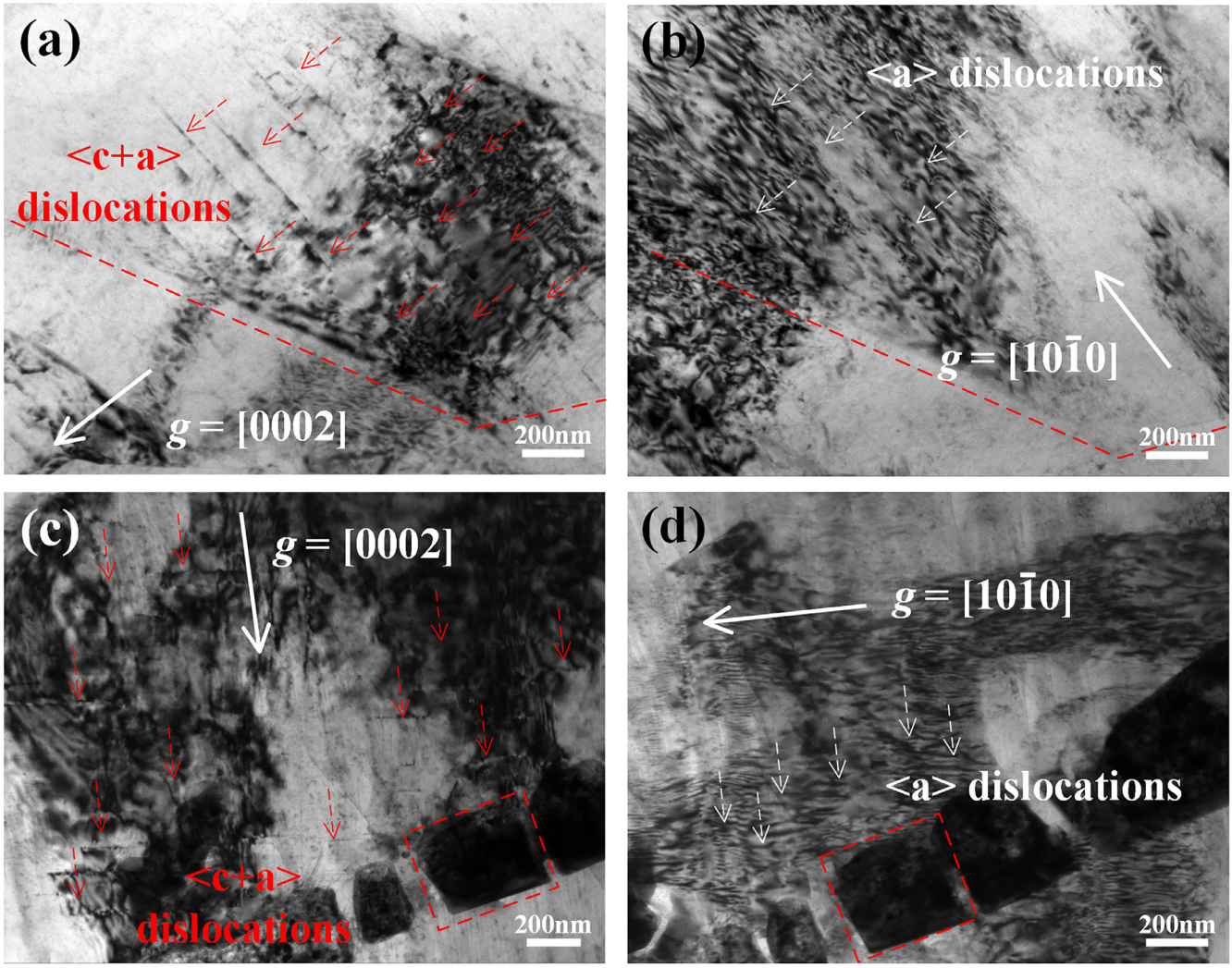

Fig. 15. BF of as-rolled (a-b) ATXS3110 and (c-d) ATXS3110-0.2Mn alloys near the [11$\bar{2}$0] zone with diffraction vectors **g** of [10$\bar{1}$0] and [0002]. To ensure that the TEM maps with different diffraction vectors are at the same location, the markers used to locate are marked in the map with red dashed lines.

the texture intensity of ~14.2 mrd and ~11.3 mrd (Fig. 14(c) and (f)), respectively. In contrast, the texture intensity of both alloys fabricated by high temperature rolling (450 °C) is ~5.3 mrd and ~4.7 mrd, respectively (Fig. 4(c) and (f)). It can be concluded that high temperature rolling is essential for the formation of a weak texture in ATXS3110 and ATXS3110-0.2Mn alloys. In addition, the role of Mn in texture weakening is more pronounced for samples rolled at 350 °C. Since the fact that non-basal slip is more difficult to activate at lower temperatures, the promoting effect of Mn on non-basal slip plays a more important role.

To explore the reason for texture weakening, bright-field (BF) images near the [11$\bar{2}$0] zone with diffraction vectors (g) of [10$\bar{1}$0] and [0002] of ATXS3110 and ATXS3110-0.2Mn alloys rolled at 450 °C were shown in Fig. 15. To ensure the same location of the TEM maps with different diffraction vectors, the markers used to locate are marked in the BF maps with red dashed lines. According to the criterion that dislocations are not visible when $\mathbf{g} \cdot \boldsymbol{b} = \mathbf{0}$, <a> dislocations are only visible with $\boldsymbol{g} = [10\bar{1}0]$, while $<c + a>$ dislocations are visible with both $\boldsymbol{g} = [10\bar{1}0]$ and $\boldsymbol{g} = [0002]$. Both alloys contain a large number of $<c + a>$ dislocations after high temperature rolling. Grains containing $<c + a>$ dislocations will induce nucleation and growth of non-basal oriented grains during annealing [23]. Therefore, the main reason for the texture weakening is the activation of numerous $<c + a>$ slip during high temperature rolling in both alloys. Moreover, it reflects that the addition of Mn has little effect on the dislocation activity of ATXS3110 alloy during high-temperature rolling.

4.2. Reasons for the excellent formability, strength and ductility

In the present work, the addition of Mn contributes to improve the strength and ductility simultaneously. As mentioned above, the addition of Mn increases the number of nano-sized phases (Figs. 7 and 8) and decreases the grain size (Fig. 4(b) and (e)). Thus, the increase in strength is mainly attributed to the enhanced grain boundary strengthening and precipita-

tion strengthening, based on Hall-Petch relation and Orowan strengthening mechanism [59,70-72]. Moreover, the decreasing grain size could inhibit the twinning activity and promote the uniform deformation, thus preventing the stress concentration [73]. Therefore, this fine-grained ATXS3110-0.2Mn alloy containing high-density nano-sized phases is expected to achieve the synergy of high ductility and strength.

With trace Mn addition, the I.E. value remarkably increases from ~5.4 mm to ~8.1 mm. It is mentioned that the addition of Mn only slightly reduces the texture intensity from ~5.3 mrd to ~4.7 mrd (Fig. 4(c) and (f)), and the area fraction of second phase in two alloys are similar, i.e., ~7.6% vs. ~7.2% (Fig. 5(a) and (c)). Therefore, neither the weakening of texture nor the variation of second phase is the main reason for the enhanced formability. It is evident that the increase of I.E. values is closely related to the grain refinement with Mn addition (from ~7.6 μm to ~4.1 μm), which results in the change of twinning behavior. Nakata et al. [29] reported that the activation of extension twin has a great influence on the evolution of texture. Owing to the larger grain size of Mn-free alloy, at the early stage of stretch forming, the fraction of extension twin boundaries to total grain boundaries at bottom half is significantly higher (~25.1%), compared to only ~3.1% in Mn-containing alloy (Fig. 9(j) and (l)). As mentioned above, the grains with the larger deviation in angle of c-axis from ND are more likely to activate extension twins and the c-axis of extension twins is closer to ND (Fig. 12). Therefore, the higher fraction of extension twins in Mn-free alloy contributes to the formation of strong basal texture (Fig. 11(a) and (e)). However, for Mn-containing alloy, the significant grain refinement could suppress the activity of extension twinning, thus inhibiting the formation of strong basal texture (Fig. 11(g) and (h)), eventually improving the formability.

5. Conclusions

In summary, the effect of trace Mn addition on the microstructural evolution and formability of ATXS3110 alloy has been systematically investigated. The formation mechanism of weak texture and the improvement mechanism of strength, ductility and formability have been revealed. The main conclusions can be drawn as follows:

(1) The origin of the formation of RD-split weak basal texture in ATXS3110 alloy is mainly attributed to the activation of large amounts of $<c + a>$ slip during high temperature rolling, which promotes the nucleation and growth of non-basal oriented grains during subsequent annealing.
(2) By trace Mn addition, the I.E. value of ATXS3110 alloy apparently increases from ~5.4 mm to ~8.1 mm. The improved formability is mainly attributed to the grain refinement (from ~7.6 μm to ~4.1 μm) via trace Mn addition, which suppresses the twinning activity during stretch forming, thus inhibiting the formation of strong basal texture.
(3) ATXS3110-0.2Mn alloy exhibits the synergy of a high ductility (EF of ~26.7%) and strength (UTS of ~254 MPa). The great ductility is closely related to the suppression of twinning induced by grain refinement. The enhanced strength is attributed to finer grain size and high-density nano-sized CaMgSn and Al_8Mn_4Ca phases.

Declaration of competing interest

The authors declare that they have no known competing financial interests or personal relationships that could have appeared to influence the work reported in this paper.

CRediT authorship contribution statement

Shi-Chao Wang: Writing – original draft, Data curation, Conceptualization. **Si-Yu Chen:** Methodology. **Zhong-Zheng Jin:** Writing – original draft, Visualization, Validation, Supervision, Methodology, Data curation, Conceptualization. **Xiao Ma:** Visualization. **Hai-Long Jia:** Methodology. **Jia-Ning Zhu:** Methodology, Conceptualization. **Chun-Yuan Li:** Investigation, Data curation. **Min Zha:** Writing – original draft, Visualization, Validation, Supervision, Methodology, Conceptualization. **Hui-Yuan Wang:** Supervision, Resources, Data curation, Conceptualization.

Acknowledgements

This work was primarily supported by The National Natural Science Foundation of China (under Nos. 52234009, U19A2084, 52171116, U22A20109, 52201113). Partial financial support came from Program for the Central University Youth Innovation Team (419021423505), the Fundamental Research Funds for the Central Universities (No. 2412022QD037), the Excellent Youth Program of Jilin Provincial Department of Education (JJKH20241425KJ) and the Fundamental Research Funds for the Central Universities, JLU.

References

[1] F. Lou, K. Liu, J.X. Liu, H.W. Dong, S.B. Li, W.B. Du, Acta Metall. Sinica 59 (11) (2023) 1439–1447.
[2] Y.K. Li, M. Zha, J. Rong, H.L. Jia, Z.Z. Jin, H.M. Zhang, P.K. Ma, H. Xu, T.T. Feng, H.Y. Wang, J. Mater. Sci. Technol. 88 (2021) 215–225.
[3] K. Guan, J.H. Zhang, Q. Yang, B.S. Li, R.Z. Wu, J. Meng, Trans. Nonferr. Metal Soc. 33 (1) (2023) 46–58.
[4] K. Guan, C. Li, Z.Z. Yang, Y.S. Yu, Q. Yang, W.W. Zhang, Z.P. Guan, C. Wang, M. Zha, H.Y. Wang, J. Magnes. Alloys (2023).
[5] Z.Z. Jin, M. Zha, S.Q. Wang, S.C. Wang, C. Wang, H.L. Jia, H.Y. Wang, J. Magnes. Alloys 10 (5) (2022) 1191–1206.
[6] Z.Z. Jin, M. Zha, H.Y. Wang, J.G. Ma, Y.C. Liu, Mater. Des. 234 (2023) 112345.
[7] K. Guan, D. Egusa, E. Abe, J. Magnes. Alloys 10 (6) (2022) 1573–1580.
[8] T. Wang, M. Zha, Y.P. Gao, S.Q. Wang, H.L. Jia, C. Wang, H.Y. Wang, Int. J. Plast. 170 (2023) 103766.
[9] D.W. Wang, K.J. Dong, Z.Z. Jin, K. Guan, F.Y. Cao, H. Zhao, M. Zha, H.Y. Wang, J. Alloys Compd. 914 (2022) 165325.
[10] H. Zhang, H.Y. Wang, J.G. Wang, J. Rong, M. Zha, C. Wang, P.K. Ma, Q.C. Jiang, J. Alloys Compd. 780 (2019) 312–317.
[11] H.Y. Wang, N. Zhang, C. Wang, Q.C. Jiang, Scr. Mater. 65 (8) (2011) 723–726.

[12] H.L. Ding, X.B. Shi, Y.Q. Wang, G.P. Cheng, S. Kamado, Mater. Sci. Eng. A. 645 (2015) 196–204.
[13] M. Zha, S.C. Wang, H.L. Jia, Y. Yang, P.K. Ma, H.Y. Wang, Mater. Sci. Eng. A. 862 (2023) 144457.
[14] Z.G. Li, Y. Miao, F.N. Liu, P.K. Ma, H.Y. Wang, Materialia 19 (2021) 101185.
[15] Z.G. Li, Y. Miao, H.L. Jia, R. Zheng, M.H. Wang, H.Y. Wang, Mater. Sci. Eng. A. 852 (2022) 143687.
[16] J.S. Li, M.X. Li, Z.M. Hua, Z.T. Hu, H.Y. Wang, J. Mater. Res. Technol. 19 (2022) 3088–3099.
[17] J.S. Li, M.X. Li, Z.M. Hua, Y.T. Mo, K. Guan, M. Zha, Y.P. Gao, H.Y. Wang, J. Mater. Sci. Technol. 163 (2023) 223–236.
[18] S. Liu, C. Wang, H. Ning, Z.-Y. Meng, K. Guan, H.-Y. Wang, J. Magnes. Alloys (2023).
[19] W.-x. Fan, Y. Bai, G.-y. Li, X.-y. Chang, H. Hao, Trans. Nonferr. Metal Soc. 32 (4) (2022) 1119–1132.
[20] Z.-Z. Jin, X. Ma, M. Zha, K. Guan, H.-Y. Wang, J.-G. Ma, Y.-C. Liu, J. Mater. Res. Technol. 27 (2023) 1160–1172.
[21] Z. Zhang, J. Zhang, J. Xie, S. Liu, Y. He, R. Wang, D. Fang, W. Fu, Y. Jiao, R. Wu, Mater. Sci. Eng. A. 831 (2022) 142259.
[22] J.-C. Chen, M.-X. Li, Z.-Y. Yu, Z.-Y. Meng, C. Wang, Z.-Z. Yang, H.-Y. Wang, J. Magnes. Alloys 11 (1) (2023) 348–360.
[23] M.Z. Bian, X.S. Huang, Y. Chino, Acta Mater. 220 (2021) 117328.
[24] X.S. Huang, K. Suzuki, Y. Chino, M. Mabuchi, J. Alloys Compd. 509 (28) (2011) 7579–7584.
[25] R.K. Sabat, A.P. Brahme, R.K. Mishra, K. Inal, S. Suwas, Acta Mater. 161 (2018) 246–257.
[26] W. Yuan, S.K. Panigrahi, J.Q. Su, R.S. Mishra, Scr. Mater. 65 (11) (2011) 994–997.
[27] T. Nakata, C. Xu, S. Kamado, Mater. Sci. Eng. A. 772 (2020) 138690.
[28] Y. Chino, K. Kimura, M. Mabuchi, Acta Mater. 57 (5) (2009) 1476–1485.
[29] T. Nakata, C. Xu, H. Ohashi, Y. Yoshida, K. Yoshida, S. Kamado, Scr. Mater. 180 (2020) 16–22.
[30] X.S. Huang, Y. Chino, M. Mabuchi, M. Matsuda, Mater. Sci. Eng. A. 611 (2014) 152–161.
[31] Z.Z. Jin, M. Zha, H.L. Jia, P.K. Ma, S.Q. Wang, J.W. Liang, H.Y. Wang, J. Mater. Sci. Technol. 81 (2021) 219–228.
[32] M. Zha, J.W. Liang, H. Xing, H. Xu, B. Jiang, C. Wang, H.L. Jia, H.Y. Wang, Mater. Sci. Eng. A. 834 (2022) 142598.
[33] N. Xia, C. Wang, Y.P. Gao, Z.M. Hua, C.Y. Ma, C.F. Du, H. Zhang, H.M. Zhang, M.X. Li, M. Zha, H.Y. Wang, Mater. Sci. Eng. A. 813 (2021) 141128.
[34] Y. Chino, K. Sassa, M. Mabuchi, Mater. Sci. Eng. A. 513-514 (2009) 394–400.
[35] Y. Chino, K. Sassa, M. Mabuchi, Mater. Trans. 49 (12) (2008) 2916–2918.
[36] Y. Chino, X.S. Huang, K. Suzuki, K. Sassa, M. Mabuchi, Mater. Sci. Eng. A. 528 (2) (2010) 566–572.
[37] T. Nakata, C. Xu, Y. Uehara, T.T. Sasaki, S. Kamado, J. Alloys Compd. 782 (2019) 304–314.
[38] D.H. Kang, D.W. Kim, S. Kim, G.T. Bae, K.H. Kim, N.J. Kim, Scr. Mater. 61 (7) (2009) 768–771.
[39] D. Wu, R.S. Chen, E.H. Han, J. Alloys Compd. 509 (6) (2011) 2856–2863.
[40] D.H. Song, T. Zhou, J. Tu, L.X. Shi, B. Song, L. Hu, M.B. Yang, Q. Chen, L.W. Lu, J. Mater. Process. Technol. 259 (2018) 380–386.
[41] T. Nakata, T. Matsuno, R. Oki, S. Kamado, J. Alloys Compd. 938 (2023) 168519.
[42] X.S. Huang, K. Suzuki, A. Watazu, I. Shigematsu, N. Saito, J. Alloys Compd. 470 (1) (2009) 263–268.
[43] U.M. Chaudry, Y.S. Kim, K. Hamad, Mater. Lett. 238 (2019) 305–308.
[44] H. Zhang, W.L. Cheng, J.F. Fan, B.S. Xu, H.B. Dong, Mater. Sci. Eng. A. 637 (2015) 243–250.
[45] J.R. Dong, D.F. Zhang, Y.F. Dong, S.S. Chai, F.S. Pan, Mater. Sci. Eng. A. 618 (2014) 262–270.
[46] X.S. Huang, K. Suzuki, N. Saito, Scr. Mater. 60 (8) (2009) 651–654.
[47] H. Zhang, G.S. Huang, J.H. Li, L.F. Wang, H.J. Roven, J. Alloys Compd. 563 (2013) 150–154.
[48] M.Z. Bian, T.T. Sasaki, B.C. Suh, T. Nakata, S. Kamado, K. Hono, Scr. Mater. 138 (2017) 151–155.
[49] T. Nakata, C. Xu, N.A.S. binti Osman, L. Geng, S. Kamado, J. Alloys Compd. 910 (2022) 164752.
[50] M.Z. Bian, T.T. Sasaki, T. Nakata, S. Kamado, K. Hono, Mater. Sci. Eng. A. 730 (2018) 147–154.
[51] B.Q. Shi, Y.H. Xiao, X.L. Shang, Y.Q. Cheng, H. Yan, Y. Dong, A.F. Chen, X.L. Fu, R.S. Chen, W. Ke, Mater. Sci. Eng. A. 746 (2019) 115–126.
[52] Q.H. Wang, H.W. Zhai, L.T. Liu, H.B. Xia, B. Jiang, J. Zhao, D.L. Chen, F.S. Pan, J. Magnes. Alloys 10 (9) (2022) 2588–2606.
[53] S. Zhou, A. Tang, T. Liu, Y. Huang, P. Peng, J. Zhang, N. Hort, R. Willumeit-Römer, F. Pan, J. Alloys Compd. 947 (2023) 169669.
[54] P. Peng, J. She, Q. Yang, S. Long, A. Tang, J. Zhang, Q. Dai, F. Pan, J. Alloys Compd. 935 (2023) 168008.
[55] P. Peng, A. Tang, B. Wang, S. Zhou, J. She, J. Zhang, F. Pan, J. Mater. Res. Technol. 15 (2021) 1252–1265.
[56] C. Tantardini, A.R. Oganov, Nat. Commun. 12 (1) (2021) 2087.
[57] X. Luo, Z.Q. Feng, T.B. Yu, J.Q. Luo, T.L. Huang, G.L. Wu, N. Hansen, X.X. Huang, Acta Mater. 183 (2020) 398–407.
[58] S.J. Chen, Q. Yu, Scr. Mater. 163 (2019) 148–151.
[59] X. Ma, M. Zha, S.Q. Wang, Y. Yang, H.L. Jia, D. Gao, C. Wang, H.Y. Wang, J. Magnes. Alloys (2022) in press.
[60] D. Zhao, X. Ma, A. Srivastava, G. Turner, I. Karaman, K.Y. Xie, Acta Mater. 207 (2021) 116691.
[61] K. Wei, R. Hu, D.D. Yin, L.R. Xiao, S. Pang, Y. Cao, H. Zhou, Y.H. Zhao, Y.T. Zhu, Acta Mater. 206 (2021) 116604.
[62] Y.K. Li, M. Zha, H.L. Jia, S.Q. Wang, H.M. Zhang, X. Ma, T. Tian, P.K. Ma, H.Y. Wang, J. Magnes. Alloys 9 (5) (2021) 1556–1566.
[63] D.K. Guan, W.M. Rainforth, L. Ma, B. Wynne, J.H. Gao, Acta Mater. 126 (2017) 132–144.
[64] Q.H. Wang, B. Jiang, A.T. Tang, J. Fu, Z.T. Jiang, H.R. Sheng, D.F. Zhang, G.S. Huang, F.S. Pan, J. Mater. Sci. Technol. 43 (2020) 104–118.
[65] N. Stanford, M.R. Barnett, Mater. Sci. Eng. A. 496 (1) (2008) 399–408.
[66] J.Y. Lee, Y.S. Yun, B.C. Suh, N.J. Kim, W.T. Kim, D.H. Kim, J. Alloys Compd. 589 (2014) 240–246.
[67] Z.Z. Jin, X.M. Cheng, Z. Min, R. Jian, Z. Hang, J.G. Wang, W. Cheng, Z.G. Li, H.Y. Wang, J. Mater. Sci. Technol. 35 (9) (2019) 2017–2026.
[68] M.N. Zhang, H.L. Jia, M. Zha, L. Zhao, Z.M. Hua, C. Wang, Y.P. Gao, H.Y. Wang, Mater. Res. Lett. 11 (9) (2023) 781–788.
[69] Z.R. Zeng, Y.M. Zhu, S.W. Xu, M.Z. Bian, J.F. Nie, Acta Mater. 105 (2016) 479–494.
[70] Z.Z. Jin, M. Zha, Z.Y. Yu, P.K. Ma, Y.K. Li, J.M. Liu, H.L. Jia, H.Y. Wang, J. Alloys Compd. 833 (2020) 155004.
[71] C.Q. Liu, X.H. Chen, D. Tolnai, Y.B. Hu, W. Zhang, Y.S. Zhang, F.S. Pan, J. Mater. Sci. Technol. 144 (2023) 70–80.
[72] M. Zha, T. Tian, H.L. Jia, H.M. Zhang, H.Y. Wang, J. Mater. Sci. Technol. 140 (2023) 67–78.
[73] R.X. Zheng, J.P. Du, S. Gao, H. Somekawa, S. Ogata, N. Tsuji, Acta Mater. 198 (2020) 35–46.